Signal denoising and viral particle identification in wide-field photon scattering parametric images using deep learning

HANWEN ZHAO,[1,4] BIN NI,[1,4] WEIPING LIU,[1] XIAO JIN,[1] HENG ZHANG,[1] BIN XU,[1] XIAOHONG W. GAO,[2] XUESONG WEN,[2] DAMING SHI,[3] JICHUAN XIONG,[1,*] AND XUEFENG LIU,[1,*]

[1]School of Electronic and Optical Engineering, Nanjing University of Science and Technology, Nanjing 210094, P. R. China

[2]Department of Computer Science, Middlesex University, London NW4 4BT, UK

[3]College of Computer Science and Software Engineering, Shenzhen University, China

[4]These authors contributed equally to this work

* correspondence: Jichuan.xiong@njust.edu.cn, liuxf_1956@sina.com

Abstract: Polarization parametric indirect microscopic imaging (PIMI) can obtain anisotropic nanoscale structural information of the sample by utilizing a polarization modulated illumination scheme and fitting the far-field variation of polarization states of the scattered photons. The rich scattering information of PIMI images can be exploited for identification of viral particles, aiming for early infection screening of viruses. Accurate processing and analysis of PIMI results is an important part of obtaining structural feature information of virus. Under noisy conditions, however, manually identifying viral particles in PIMI images is a very time-consuming process with a high error rate. The systematic noise degrading the image resolution and contrast are mainly due to the mechanical or electrical disturbance from the modulation of the illumination when taking raw images. To achieve efficient noise suppressing and accurate virus identification in PIMI images, we developed a neural network-based framework of algorithms. Firstly, a fairly effective denoising method particularly for PIMI imaging was proposed based on a generative network. Both the numerical and experimental results show that the developed method has the best capability of noise removal for PIMI images compared with the traditional denoising algorithms. Secondly, we use a convolutional neural network to detect and recognize viral particles in PIMI images. The experimental results show that viral particles can be identified in PIMI images with high accuracy.

1. Introduction

In the past few years, a far-field super-resolution imaging method called polarization parametric indirect microscope imaging (PIMI) has been developed [1], indicating the capability of perceiving the spatial scattering distribution beyond the diffraction limit and resolving the sub-wavelength features of the sample [2]. PIMI provides a series of parametric images which reflects the detailed nanoscale properties of the sample which is unable to be uncovered in conventional microscopes. Therefore, it has been effectively applied for investigating the morphological and structural features of graphene layers[1], nano-particles [2] and nanopores[11]. PIMI system has been proved to be able to obtain information about nanostructures, making it possible to screen for the early infection by detection of viral particles with an optical system.

Viruses pose a huge threat to public health and the ability to detect them rapidly is of great

importance for tracking and preventing pandemics such as COVID-19 []. Though much is now known about the biological and pathogenic properties of many viruses, their ability to mutate quickly and the emergence of new infection agents can make it difficult to detect them rapidly []. Many virus detection methods have been developed. Indirect methods include: analysis of viral ribonucleic acid (RNA) based on the Reverse Transcription-Polymerase Chain Reaction (qRT-PCR), polymerase chain reaction (PCR) and enzyme-linked immunosorbent assay (ELISA) []; Loop-mediated isothermal amplification (LAMP) []; the CRISPR/Cas System []. Direct detection of the intact viral particles is more straightforward and shows potential for fast virus-screening applications [].

Compared with methods above, detection of intact viral particles with optical sensing methods is more convenient and cost-effective. The absorption spectrum of aggregated AuNPs around virus-like particles (VLPs) has been utilized to detect the viruses []. Recently, portable platforms based on Raman spectroscopy have been developed to identify viral particles by analyzing their sizes []. Due to the convenience and cost-effectiveness of optical methods, it make sense to utilize the nanoscale structural resolving ability of PIMI for virus detection. Accurate processing and analysis of PIMI images is an important part of obtaining structural feature information of virus. However, due to the presence of noise, manual recognition of PIMI images is time-consuming and the accuracy cannot be guaranteed. Hence, designing a powerful denoising method particularly for PIMI is urgent and valuable.

In order to obtain a series of polarization parametric images, such as the phase retardance δ of orthogonal components, the orientation angle φ of the polarization ellipticity, and Stokes parameters S_0, S_1, S_2 and S_3, the PIMI system captures a set of raw images while modulating the illumination polarization, and the far-field pixel intensity variation were fitted and filtered to calculate the parametric images. In this procedure, the final calculation result is heavily dependent on the quality of raw images, which is usually inevitably degraded by the noise from the modulation module, especially when imaging nanoscale samples with large magnification objectives. The presence of noise in the PIMI intensity images not only degrades the image quality, but also leads to the reconstruction errors of the parametric images.

Currently, many denoising algorithms [12-16] has been developed which are suitable to be used in conventional microscopy imaging but not fully appropriate for PIMI as the latter has its special way of data retrieving and calculation, which will be introduced in the following part. Actually, even if we perform denoising on all the raw images in PIMI, the residual noise will also be introduced into the polarization result and even magnified by the reconstruction procedure of the polarization parameters. This issue becomes even worse when imaging nanoscale samples below the diffraction limit, such as nano-particles or nanopores. In some polarization imaging methods, such as division of focal plane (DoFP) polarimeters, specialized denoising algorithms [17-19] are designed, which however cannot be directly applied to PIMI because of their notably different measuring and reconstruction procedures. Besides, deep learning methods [20-23] are also widely used for image denoising while they typically require a huge training data sets, and it is difficult and impractical to make a sufficient amount of ground truth data in PIMI.

There are many image denoising algorithms such as NLM [] and bm3d [30] that use the self-similarity of the image to denoise and have achieved good results. Lempitsky et al. [24] proved that neural networks also have the ability to learn the self-similarity of images. These methods show good potential to be utilized for denoising the PIMI images.

In this paper, based on the generative network, we utilize self-similarity of image and propose a highly efficient denoising method specifically targeted at PIMI imaging for the first time. Firstly, we construct a convolutional neural network. Secondly, we use a random code vector as the input of network to learn the noisy PIMI image, and utilize Mean Squared Error (MSE) as cost function to train the network parameters. Finally, when the network iterates to a certain number of epoch, we can get the PIMI image with noise suppressed. Both simulated and real PIMI images are employed to evaluate the denoising performance. Results prove that we

have combined deep learning and PIMI system well and the proposed method can effectively suppress noise and improve resolution while preserving the characteristics of the PIMI scattering distribution. Moreover, we try to use another convolutional neural network [] to detect and recognize viral particles in PIMI images and experimental results show that PIMI can be well applied to virus detection and identification.

2. Method

2.1 PIMI method

PIMI system is built by modifying a conventional optical far field microscopy such that the variation of the polarization status of the incident light can be precisely controlled. When this linear polarized beam with different polarization angles impinges on sample under test (SUT), it collects different information depending on the atomic arrangement of the SUT.

We rotate the linear polarization field from 0° to 360°, so, we can express the intensity of the complete modulation process as [25,26]:

$$I = \frac{I_0}{2}[1 + \sin 2(\alpha - \phi) \sin \delta \ ]. \tag{1}$$

Where I_0 is the non-polarized intensity, α is the input polarization angle, ϕ is the angle along the slow vibration axis and δ is the optical retardation (the phase shift between the E_y and E_x).

If we expand Eq. (1) trigonometrically, then we obtained

$$I = \frac{1}{2}I_0 + \frac{1}{2}I_0 \ \sin \delta \ \cos 2\phi \ \sin 2\alpha + \frac{1}{2}I_0 \ \sin \delta \ \sin 2\phi \ \cos 2\alpha \qquad . \tag{2}$$

We can derive the required parameters after the fitting by the following equation:

$$I_i = a_0 + a_1 \sin \alpha + a_2 \cos \alpha. \tag{3}$$

Comparison of Eq. (2) and Eq. (3) give us

$$a_0 = \frac{1}{2}I_0, a_1 = \frac{1}{2}I_0 \sin \delta \ \cos 2\phi, a_2 = -\frac{1}{2}I_0 \sin \delta \ \sin 2\phi. \tag{4}$$

If we rotate the polarization to total 360°angles, then a total number of angles are N=360° and here, a_0, a_1 and a_2 are calculated as below:

$$a_0 = \sum_{i=1}^{N} \frac{1}{N}I_i, a_1 = \sum_{i=1}^{N} \frac{2}{N}I_i \ \sin \alpha_i, a_2 = \sum_{i=1}^{N} \frac{2}{N}I_i \ \cos \alpha_i. \tag{5}$$

Using these parameters, the desired quantities can be found as:

$$I_{dp} = a_0, \sin \delta = \frac{\sqrt{a_1^2 + a_2^2}}{a_0}, \phi = \frac{1}{2}\cos^{-1} \ (\frac{a_1}{\sqrt{a_1^2 + a_2^2}}) \ . \tag{6}$$

And then, Stokes parameters can be calculated by a mutual relationship between Jones and Muller model as follows:

$$\begin{cases} S_0 = I_{dp}(1 + \sin \delta) = E_{0x}^2 + E_{0y}^2 \\ S_1 = I_{dp}(1 + \sin \delta) \cos 2\phi = E_{0x}^2 - E_{0y}^2 \\ S_2 = = E_{0x}E_{0y}^* - E_{0y}E_{0x}^* \\ S_3 = = i \ (E_{0x}E_{0y}^* - E_{0y}E_{0x}^*) \end{cases} \quad . \tag{7}$$

These Stokes parameters are calculated from the I_{dp}, $\sin \delta$, and ϕ, which are derived after the fitting and filtration process (Eq. (6)).

However, there are many disturbances throughout the process, which leads to the noisy I_i and noisy fitted polarization parameters. Traditional denoising methods operate on a single picture, but the PIMI image is the result of calculation and fitting of multiple original images, which makes the noise more disordered. Obviously, traditional denoising methods can no longer suitable for PIMI images.
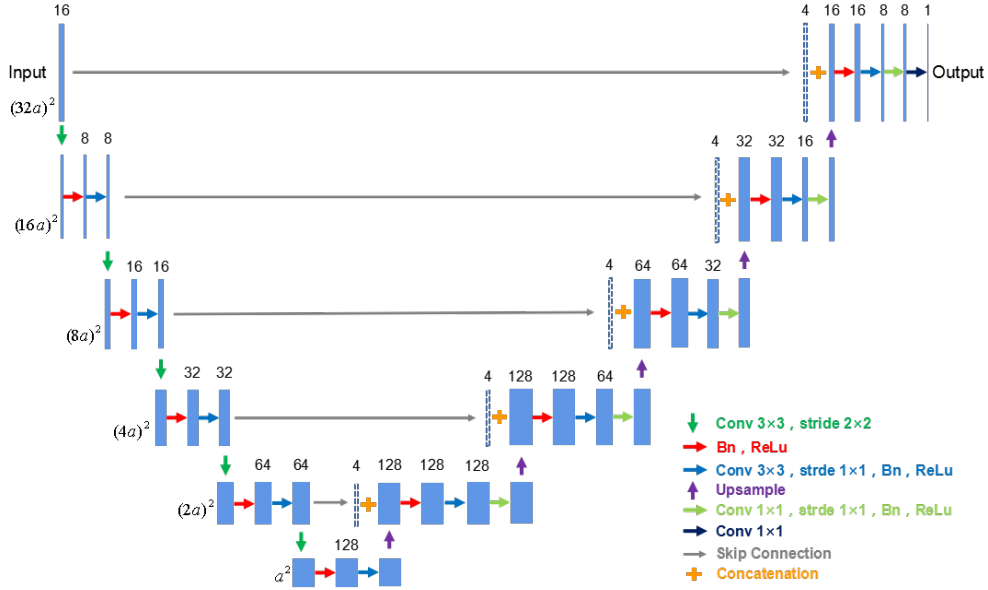
2.2 Denoising for PIMI images

Fig. 1. Network architecture. Each blue box corresponds to a multi-channel feature map. The number of channels is provided on top of the box. The x-y-size is denoted at the lower left edge of the box. White-dotted boxes represent copied feature maps. The arrows and symbol denote different operations.

Assume that an observed noisy PIMI intensity image I_i^n is generated by adding Gaussian noise n_i to the noise-free image I_i, as formulated by Eq. (8):

$$I_i^n = I_i + n_i. \tag{8}$$

where $n_i \sim N(0, \sigma_i^2)$ is a Gaussian noise with zero mean and the standard deviation σ_i, for i is 0° to 360°.

Thus, the fitting process of PIMI can be written as follows:

$$x^n = F(I_i^n) \tag{9}$$

where F() is fitting process and x^n represent all PIMI polarization parameters with noise.

In order to achieve denosing function, we construct a convolutional neural network. The architecture of neural network is inspired by U-Net [27], as shown in Fig. 1. It is comprised of a down-sampling path in the left side, an up-sampling path in the right side, and two bridge paths in the middle to connect the down- and up-sampling paths. The down-sampling path consists of five repeated stages of two 3×3 convolutions with stride 2, 1. The number of feature channels is increased by the first convolution in each stage of down-sampling path (the first stage is from 16 channels to 8 channels and the rest stages double the channels). The bridge path is gained by extracting the feature map through the convolution from the down sampling path. The up-sampling path consists of five repeated stages of an up-sample concatenating with corresponding feature map at the down-sampling path by skip connection and two 3×3 convolutions with stride 1. The last convolutions in each stage of up-sampling path decrease the number of the feature channels (the last stage is from 8 channels to 1 channel and the rest stages halve the channels). All the convolutions in this neural network are followed by a BN and a ReLU for faster training speed and non-linear ability [28,29].

The denoising process is shown in Fig. 2. We use a random code vector $\mathcal{Z}$ as the input of the network which is mapped to a polarization parameter x:

$$x = f_\theta(\mathcal{Z})$$

(10) where $f_\theta()$ is parameterization of the network and $x \in \mathbb{R}^{1 \times H \times W}$, $\mathcal{Z} \in \mathbb{R}^{3 \times H \times W}$.
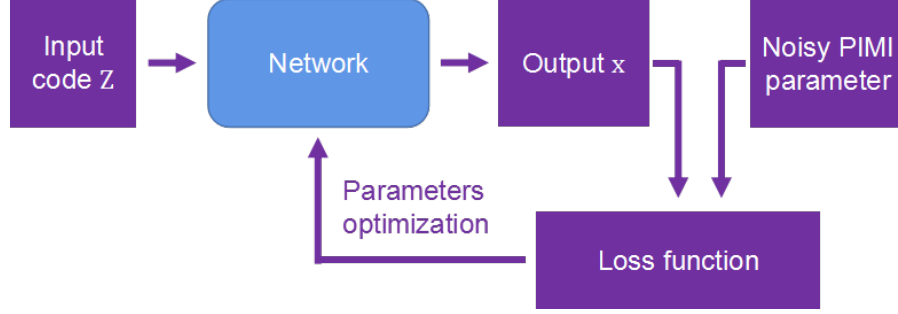
Fig. 2. Network denoising flow diagram

Noisy PIMI image x^n is regarded as our ground truth and we aim to generate it through Z, so mean squared error (MSE) is a suitable loss function:

$$E(x; x^n) = \|x - x^n\|^2 \tag{11}$$

Next, the loss function is back-propagated through the network and the ADAM-based optimization with a learning rate of 0.01 is adopted to update the network's parameters:

$$\theta^* = \underset{\theta}{\operatorname{argmin}} \|f_\theta(Z) - x^n\|^2 \tag{12}$$

It is worth noting that we always learn the original parameter x instead of image of x to reduce the error introduced by parameter visualization. We utilize the network's priori and self-similarity of the parametric image to reduce the noise and improve the resolution of the PIMI images. The generative network can learn the undamaged part of the image x^n first, and then learn the damaged part. Generation of noisy PIMI parameter is undesired, thus we need to stop iteration process before the noisy points be learned by network. Finally, after an appropriate number of iterations, the denoised PIMI parameters can be gained.

2.3 *Viral particle detection and recognition in PIMI images*

Faster-RCNN is applied in this task which demonstrated excellent performance in the field of object detection and recognition. At this time, we employ it to identify viral particles in PIMI image. In our work, three different particles present in the same sample — single AuNPs (antibody-conjugated gold nanoparticles), double AuNPs and AuNPs-virus, which size is about 100nm. In order to get the accurate position and category of all particles on the PIMI images, as we call ground truth, we collect scanning electron microscopic (SEM) images of all samples. By referring to the SEM images, the ground truth is obtained.

3. Denoising experimental setup and results
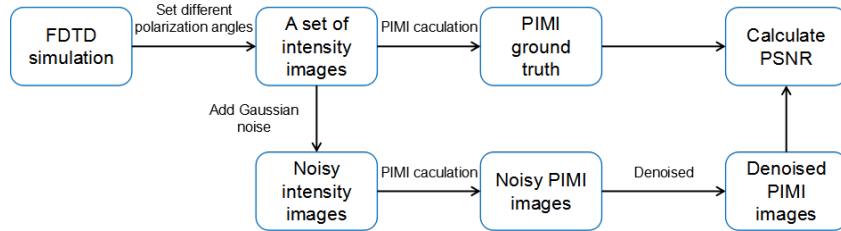
3.1 Experimental setup

Fig. 3. Experiment flow diagram

Experiment process is shown in Fig. 3. In order to get a series of noise-free PIMI intensity data

in different polarization orientations, we apply finite difference time domain (FDTD) software to simulate. Three different objects are designed and the wavelength of incident light is set to 532nm which is the same as real experimental conditions. By setting the incident light to linearly polarized light and rotating the polarization orientations from 0° to 180° offset by 18°, we generate 10 intensity images (320×320 pixel and one pixel represent 34.5nm×34.5nm). After performing inversion calculation on these 10 images as mentioned in section 2, we get noise-free simulated PIMI polarization parameter. Next, we save the intensity data and original parameter data. Then, we add Gaussian white noise to the 10 simulated noise-free intensity data respectively and calculated noisy PIMI parameters. Finally, to evaluate the denoising performance, a comparison between our method and other effective ones are made, and the compared figures of merit are included. Real PIMI images are recorded by our self-developed PIMI microscope system. The $\sin\delta$ and ϕ images are selected for visual comparison and the simulated data of the measured object is used as reference.

3.2 Experimental results

In this section, visual comparison and PSNR analysis are applied to the simulated PIMI images. Moreover, real PIMI images are used to illustrate differences visually. For implementing the network, Pytorch framework based on Python 3.7.4 is used. The proposed method is performed on a workstation with Intel(R) Xeon(R) Gold 6126 CPU @2.60GHz and 512GB of RAM, using NVIDIA Quadro P600 GPU. In order to ensure the integrity of denoising results, the size of the parameter data should be an integer multiple of 32. Our network has more than five hundred thousand parameters. With the help of GPU, the training process takes ～12s for 100 epochs. Notice that we only train on one parameter datum, so we don't need a testing process. The number of training epoch we choose is 3000.

3.2.1 Results on simulated PIMI images

As shown in Fig. 4, three still intensity images (polarization angle is 0°) with spatial resolution of 320×320 and gray-level of 8 bit were simulated to evaluate the performance of the proposed method and compare with the traditional denoising algorithms, which include the average filtering, Wiener filtering, median filtering, bm3d [30] and ksvd [31].
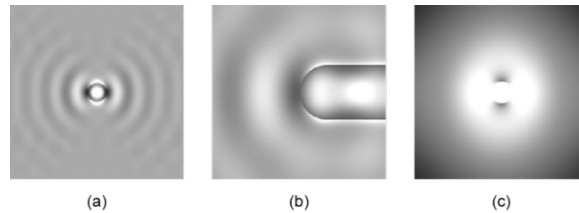

Fig. 4. Three intensity images: (a) Polystyrene ball; (b) Acetobacter xylinum; and (c) Nanopore.
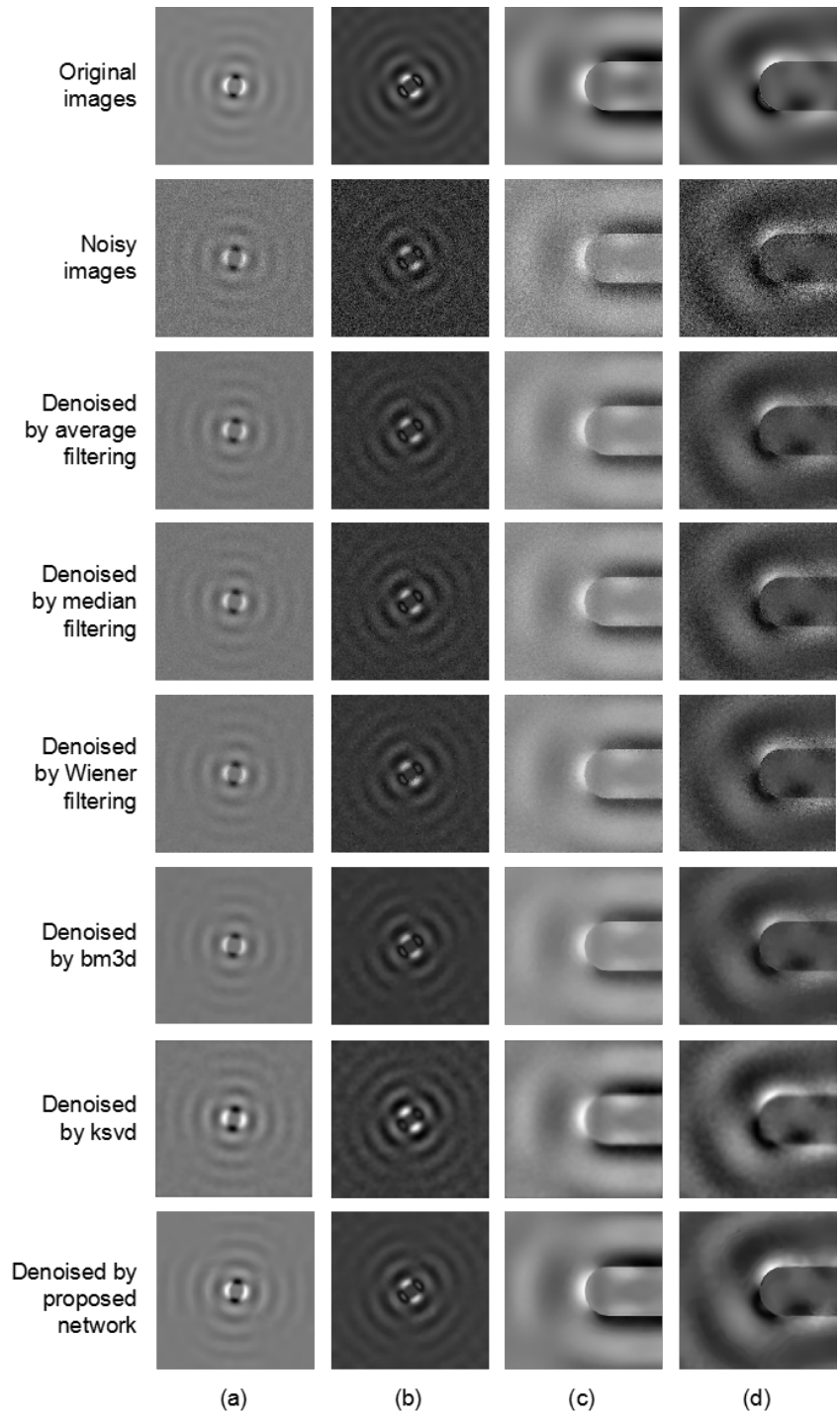
Fig. 5. Denoising results for simulated PIMI images:(a) Polystyrene ball's $\sin\delta$ image; (b) Polystyrene ball's ϕ image; (c) Acetobacter xylinum's $\sin\delta$ image; and (d) Acetobacter xylinum's ϕ image.

Denoising result for simulated PIMI images are shown in Fig. 5. Different columns present $\sin\delta$ and ϕ images of different objects. The original images in the first row are calculated

from ten intensity images which were simulated by FDTD. The original images are used to visually compare the denosing results and as the noise-free images to calculate the PSNR. The second row presents noisy $\sin\delta$ and ϕ images. They are reconstructed as following: we firstly add Gaussian noise to ten intensity images separately with $\sigma = 0.01$ before the inversion calculation. Next, we perform inversion calculation on these 10 noisy images as mentioned in section 2. Finally, $\sin\delta$ and ϕ images are reconstructed. Both the $\sin\delta$ and ϕ images are full of noise. Images from third row to seventh row show the images denoised by five different denoising methods respectively. The third through fifth rows are obtained by the traditional denoising methods, i.e. the average filtering, median filtering and Wiener filtering. From these three sets of images, it can be observed that the traditional denoising methods have no obvious effect on the polarization parameter image, even if the σ of Gaussian noise is only 0.01. The sixth row is obtained by bm3d denoising method. As shown in the sixth row, although the noise is suppressed, the image is very fuzzy and the gray level of the image is different from the original image. Using the ksvd denoising method, we get the seventh row. It is obvious that the denoised images have not been greatly improved, and the edges are blurred. The results of using our proposed denoising method are shown in the last row. The noise is effectively suppressed. Meanwhile, these images closely resemble the original images. Thus, our proposed denoising method for PIMI images can effectively mitigate noise while preserving details.

The PSNR is used as an objective evaluation criterion to analyze the denoising performance. As a result, the PSNR values of different denoising algorithms are calculated for all the test images and summarized in Table 1 and Table 2. For the test images of "Acetobacter xylinum," the study is further extend to the Gaussian noise with various standard variances and other PIMI parameters image, which is shown in Table 3 and Table 4 respectively. Table 3 shows the PSNR values of the different denoising algorithms for eliminating Gaussian noise with different standard variances. Furthermore, the curves of PSNR versus Gaussian noise with different standard variances are presented in Fig. 6. And Table 4 presents the PSNR results for all PIMI parameter images.

Based on the results in Table 1 and Table 2, when suppressing Gaussian noise with a standard variance σ equals to 0.01, the PSNR value of our proposed method outperforms the other five methods by 12.13% ~ 45.44% for ϕ image and 3.15% ~ 71.71% for $\sin\delta$ image. In Fig. 6, it can be observed that the PSNR deceases with the increment of the Gaussian noise's standard variances, and the PSNR of the proposed method still takes great advantages compared with the other methods. Based on the comparison results presented in Table 4, the PSNR results of the proposed method still outperform the other five methods for all the PIMI parameter images. There are two reasons that the proposed method can achieve the best performance in terms of PSNR: 1) PIMI images are different from natural images, and conventional denoising algorithms are not suitable. 2) More importantly, our proposed method directly denoises the parameters instead of the image of parameters.

Table 1. Different test ϕ images' PSNR values with Gaussian noise added ($\sigma = 0.01$)

PSNR(dB)	Noisy image	Average filtering	Median filtering	Wiener filtering	BM3D	KSVD	This work
Polystyrene ball	22.41	28.61	27.90	29.32	31.09	32.18	**39.51**
Acetobacter xylinum	19.31	23.29	23.01	23.45	24.47	28.94	**32.45**
Nanopore	15.71	17.24	16.99	17.08	17.41	18.85	**24.71**

Table 2. Different test $\sin \delta$ images' PSNR values with Gaussian noise added ($\sigma = 0.01$)

PSNR(dB)	Noisy image	Average filtering	Median filtering	Wiener filtering	BM3D	KSVD	This work
Polystyrene ball	25.45	27.47	28.23	28.79	29.19	29.00	**36.47**
Acetobacter xylinum	22.09	23.73	23.80	23.98	24.18	24.53	**31.38**
Nanopore	22.49	26.61	26.67	26.37	28.57	17.16	**29.47**

Table 3. PSNR comparison of "Acetobacter xylinum" $\sin \delta$ image corrupted by Gaussian noise with different standard variances

PSNR(dB)	Noisy image	Average filtering	Median filtering	Wiener filtering	BM3D	KSVD	This work
$\sigma = 0.01$	22.09	23.73	23.80	23.98	24.18	24.53	**31.38**
$\sigma = 0.026$	21.59	23.74	23.74	24.03	24.38	26.21	**28.79**
$\sigma = 0.041$	19.98	22.29	22.27	22.44	22.79	23.86	**28.89**
$\sigma = 0.057$	19.66	21.73	21.69	21.87	22.14	24.58	**27.41**
$\sigma = 0.072$	19.08	20.90	20.87	20.98	21.19	24.75	**28.42**
$\sigma = 0.088$	18.44	20.84	20.78	20.94	21.27	25.54	**26.62**
$\sigma = 0.1$	17.72	19.60	19.57	19.64	19.84	23.93	**24.99**
$\sigma = 0.12$	18.06	20.19	20.17	20.28	20.51	26.10	**28.24**
$\sigma = 0.13$	17.90	20.20	20.17	20.30	20.57	25.65	**25.77**
$\sigma = 0.15$	18.53	20.79	20.74	20.92	21.20	22.62	**27.47**

Table 4. PSNR comparison of "Acetobacter xylinum" PIMI parameter image

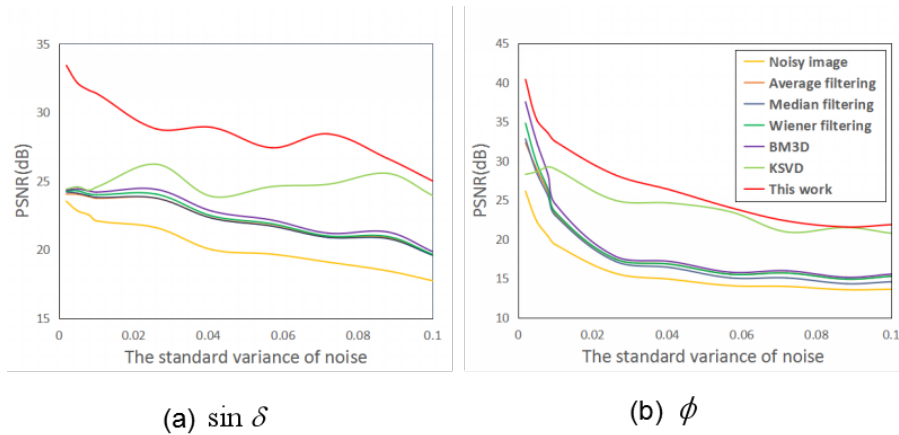| PSNR(dB)	Noisy image	Average filtering	Median filtering	Wiener filtering	BM3D	KSVD	This work
I_{dp}	35.83	36.48	41.41	43.35	45.35	11.22	**46.41**
$\sin \delta$	22.09	23.73	23.80	23.98	24.18	24.53	**31.38**
ϕ	19.31	23.29	23.01	23.45	24.47	28.94	**32.45**
S_0	22.54	24.23	24.34	24.65	24.81	26.31	**28.71**
S_1	22.30	23.93	24.02	24.30	24.45	27.02	**29.63**
S_2	21.79	30.17	28.96	31.68	36.99	21.01	**37.59**
S_3	21.15	29.50	28.31	31.19	36.55	21.35	**38.60**

(a) $\sin \delta$ (b) ϕ

Fig. 6. PSNR comparison of "Acetobacter xylinum" images corrupted by Gaussian noise with different standard variances.

3.2.2 Results on real PIMI images

Real PIMI images of 100nm single AuNPs are recorded by the PIMI system as shown in Fig. 7. The first and second columns present $\sin \delta$ and ϕ images respectively. The first row presents raw images that are almost overwhelmed by noise because of the small size. The images in the second row are obtained by using our proposed method. For comparison, we use FDTD to simulate the PIMI images of the recorded object, as shown in the third row. It can be seen that although our denoising results are not completely equivalent to the simulation results, their scattering distributions are consistent in appearance, which will benefit in the field of microscopic polarization imaging in presenting better quality detailed images.

4. Virual particles identifiction experimental setup and results

4.1 Experimental setup

Experiment process is shown in Fig. 8. First, we use the PIMI system to obtain the polarization parameter image of the virus particle. As mentioned in Section 2, there are three different types of particles in our samples. Secondly, in order to obtain the category information of each particle, we perform SEM imaging on all samples. Then, by referring to the SEM image, every particle on the sample can be identified. Next, we mark all particles on the PIMI images. All groundtruth is split into 320×320 pixel images, and divided into training set and test set. Finally, to evaluate network performance, the trained network is performed on the test set.
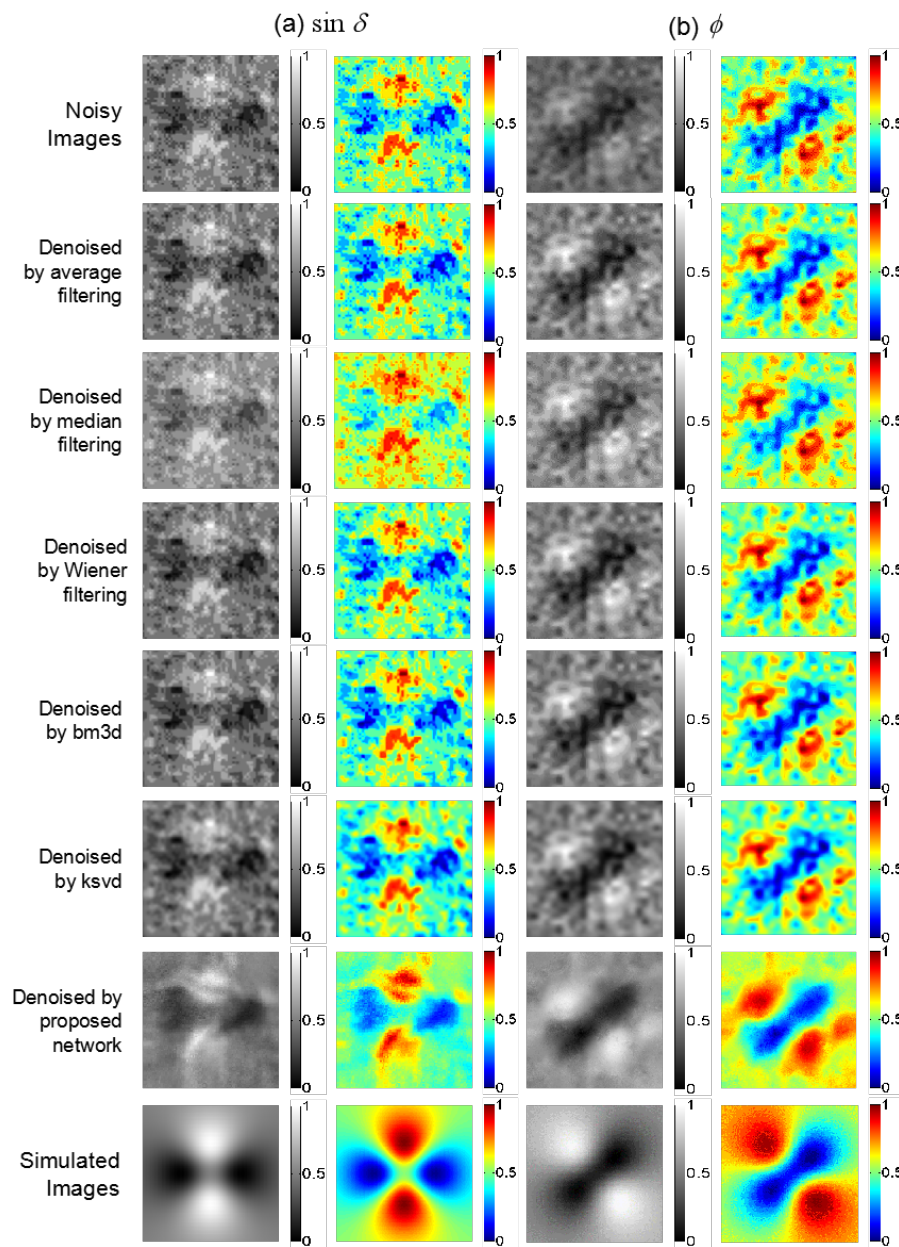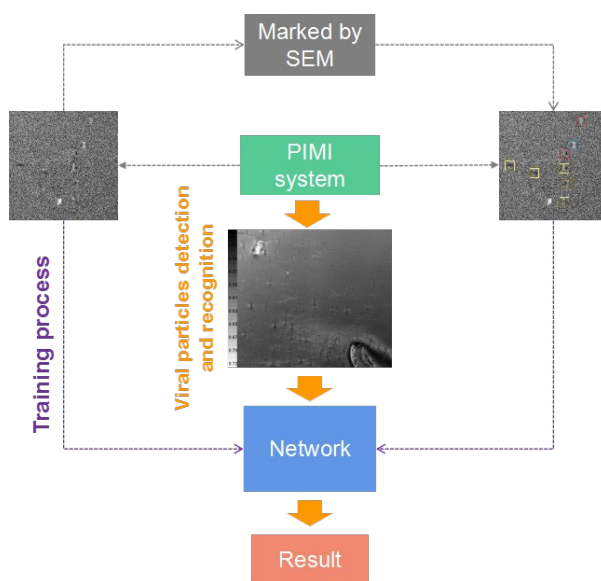
Fig. 7. Denoising results for real PIMI image.

Fig. 8. Experiment flow diagram

4.2 Experimental results

Viral particles detection and recognition results are shown in Fig. 9. As we can see, the three different particles have been detected and recognized. The picture on the left is the identification result of single AuNPs. We can see that the PIMI scattering state of single AuNPs is relatively consistent. The images in the middle and the right are the recognition results of double AuNPs and AuNPs-virus respectively. Compared with single AuNPs, their scattering states have many forms, and they are difficult to be distinguished by the human eye. Their multiple scattering states will be researched in future work. With reference to the SEM image, all the detection and recognition results shows high accuracy. The overall accuracy rate has reached 93.54%, and the AuNPs-virus identification rate has reached 94.44%.
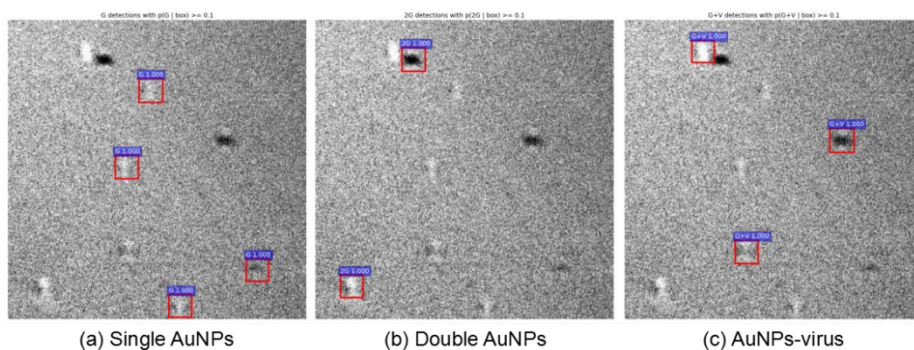

(a) Single AuNPs (b) Double AuNPs (c) AuNPs-virus

Fig. 9. Viral particles detection and recognition results

5. Conclusion

In this paper, we proposed a generative network-based denoising method specifically targeted at PIMI imaging for the first time which learn the original PIMI parameters instead of image of parameters. The priori of the generative network and the self-similarity of PIMI parameters are fully exploited during the denoising process. Both simulated and real PIMI images are used to evaluate the denoising performance. Experimental results show that PIMI image are different from natural image, and traditional denoising methods have no obvious benefit to PIMI imaging. The proposed denoising method for PIMI parameters can effectively mitigate noise and improve resolution while preserving scattering distribution characteristics. We use a convolutional neural network to detect and recognize virul particles in PIMI images and results demonstrate that viral particles can be recognized in PIMI images with high accuracy. The rich scattering information of PIMI images provides a new route for virus identification and other particle recognition applications. In denoising part, however, the optimal learning epoch for network denoising is not fixed, due to the variation of noise strength. At the same time, the parameters in PIMI such as S_0, S_1, the gray level will change greatly when noise is added, which may lead to possible degraded performance of the denoising methods. In future work, the denoising methods for PIMI images will be further improved for application in more general sceneries.

Acknowledgments

Disclosures

The authors declare no conflicts of interest.

References

1. X. Liu, B. Qiu, Q. Chen, Z. Ni, Y. Jiang, M. Long, L. Gui, "Characterization of graphene layers using super resolution polarization parameter indirect microscopic imaging," Opt. Express **22**(17), 20446-20456 (2014).
2. K. Ullah, X. Liu, H. Muhammad, Z. Shen, "Subwavelength far field imaging of nanoparticles with parametric indirect microscopic imaging," ACS Photonics **5** (4), 1388-1397 (2018).
3. G. Liu, K. Gao, G. Ni, X. Liu, "Analysis on morphological and structural features of graphene layers by using polarization indirect microscopic imaging system," International Conference on Optical Instruments and Technology (2015), pp. 96240I-96240I.
4. Z. Huang, X. Liu, L. Zhou, "Preliminary study of graphene structure by indirect imaging using polarization parameters," Acta Optica Sinica 34.B12, 183-189 (2014).
5. N.P. Yadav, X. Liu, W. Wang, K. Ullah, B. Xu, "Pattern characteristics and resolution of GaN sample through parameter of indirect microscopic imaging," In Journal of Physics: Conference Series (Vol. 844, No. 1, p. 012005), IOP Publishing (2017).
6. G. Liu, K. Gao, X. Liu, G. Ni, "Comparisons between conventional optical imaging and parametric indirect microscopic imaging on human skin detection," In 2016 International Workshop on Information Data Storage and Tenth International Symposium on Optical Storage, Int. Soc. Opt. Photon. 9818, 98180Q (2016).
7. J. Zhao, X. Liu, J. Xiong, L. Zhou, "Investigation of skin structures based on infrared wave parameter indirect microscopic imaging," Fourth International Conference on Optical and Photonics Engineering (2017), pp. 102500Q-102500Q.

8. K. Ullah, X. Liu, J. Xiong, J. Hao, B. Xu, Z. Jun, W. Liu, "A polarization parametric method of sensing the scattering signals from a submicrometer particle," IEEE Photonics Technol. Lett **29** (1), 19–22 (2017).

9. G. Liu, K. Gao, X. Liu, G. Ni, "Analysis on near field scattering spectra around nanoparticles by using parametric indirect microscopic imaging," Opt. Commun 377, 59-64 (2016).

10. K. Ullah, X. Liu, M. Habib, L. Song, N. Yadav, B. Garcia-Camara, "Light scattering by subwavelength Cu2O particles," Nanotechnology **28** (13), 134002 (2017).

11. W. Liu, J. Xiong, L. Zhu, S. Ye, H. Zhao, J. Liu, H. Zhang, L. Hou, J.H. Marsh, L. Dong, X.W. Gao, D. Shi, and X. Liu, "Characterization of deep sub-wavelength nanowells by imaging the photon state scattering spectra," Opt. Express 29, 1221-1231 (2021).

12. A. Buades, B. Coll, J. Morel, "A non-local algorithm for image denoising," Computer Vision and Pattern Recognition **2** (2), 60-65 (2005).

13. M. Elad, M. Aharon, "Image Denoising Via Sparse and Redundant Representations Over Learned Dictionaries," IEEE Trans. Image Process **15**(20), 3736-3745 (2006).

14. J. Xu, L. Zhang, W. Zuo, D. Zhang, X. Feng, "Patch Group Based Nonlocal Self-Similarity Prior Learning for Image Denoising," international conference on computer vision (2015), pp. 244-252.

15. S. Gu, L. Zhang, W. Zuo, X. Feng, "Weighted Nuclear Norm Minimization with Application to Image Denoising," Computer Vision and Pattern Recognition, 2862-2869 (2014).

16. J. Mairal, F. Bach, J. Ponce, G. Sapiro, A. Zisserman, "Non-local sparse models for image restoration," International conference on computer vision (2009), pp. 2272-2279.

17. J. Zhang, H. Luo, R. Liang, W. Zhou, B. Hui, Z. Chang, "PCA-based denoising method for division of focal plane polarimeters," Opt. Express **25**(3), 2391–2400 (2017).

18. A.B. Tibbs, L.M. Daly, N.W. Roberts, D. Bull, "Denoising imaging polarimetry by adapted BM3D method," Journal of The Optical Society of America A-optics Image Science and Vision **35**(4), 690-701 (2018).

19. W. Ye, S. Li, X. Zhao, A. Abubakar, A. Bermak, "A K Times Singular Value Decomposition Based Image Denoising Algorithm for DoFP Polarization Image Sensors With Gaussian Noise," IEEE Sensors Journal **18**(15), 6138-6144 (2018).

20. H.C. Burger, C.J. Schuler, S. Harmeling, "Image denoising: Can plain neural networks compete with BM3D?" Computer Vision and Pattern Recognition, 2392-2399 (2012).

21. X. Mao, C. Shen, Y. Yang, "Image Restoration Using Convolutional Auto-encoders with Symmetric Skip Connections," Computer Vision and Pattern Recognition, (2016).

22. K. Zhang, W. Zuo, Y. Chen, D. Meng, L. Zhang, "Beyond a Gaussian Denoiser: Residual Learning of Deep CNN for Image Denoising," IEEE Trans. Image Process **26**(7), 3142-3155 (2017).

23. J. Chen, J. Chen, H. Chao, M. Yang, "Image Blind Denoising with Generative Adversarial Network Based Noise Modeling," Computer Vision and Pattern Recognition, 3155-3164 (2018).

24. V. Lempitsky, A. Vedaldi, D. Ulyanov, "Deep Image Prior," computer vision and pattern recognition, 9446-9454 (2018).

25. A.M. Glazer, J.G. Lewis, W. Kaminsky, "An automatic optical imaging system for birefringent media," Proceedings of The Royal Society A: Mathematical, Physical and Engineering Sciences **452**(1955), 2751-2765 (1996).

26. W. Kaminsky, K. Claborn, B. Kahr, "Polarimetric imaging of crystals," Chemical Society Reviews. **33**(8), 514-525 (2004).

27. O. Ronneberger, P. Fischer, T. Brox, "U-net: convolutional networks for biomedical image segmentation," International Conference on Medical Image Computing and Computer-assisted Intervention. Springer (2015), pp. 234–241.

28. S. Ioffe, C. Szegedy. "Batch normalization: accelerating deep network training by reducing internal covariate shift," arXiv preprint arXiv. 1502.03167 (2015).

29. X. Glorot, A. Bordes, Y. Bengio, "Deep sparse rectifier neural networks," Proceedings of the Fourteen International Conference on Artificial Intelligence and Statistics (2011), pp. 315-323.

30. K. Dabov, A. Foi, V. Katkovnik, and K. Egiazarian, "Image Denoising by Sparse 3-D Transform-Domain Collaborative Filtering," IEEE Trans. Image Process 16:2080–2095 (2007).

31. M. Aharon, M. Elad, and A. Bruckstein, "K-SVD: An algorithm for designing overcomplete dictionaries for sparse representation," IEEE Trans. Signal Process **54**(11), 4311–4322 (2006)